AIChE

Probability Density Function Simulation of Turbulent Reactive Gas-Solid Flow in a FCC Riser

Suryanarayana Prasad Vegendla, Geraldine J. Heynderickx, and Guy B. Marin
Universiteit Gent, Laboratorium voor Chemische Technologie, Krijgslaan 281, S5, Gent, Belgium-9000

DOI 10.1002/aic.12569

A newly developed hybrid solution algorithm applicable on turbulent multiphase, gas-solid, reactive flows is presented. A finite volume (FV) and a probability density function (PDF) method are combined. The FV technique is used to solve the total mass and momentum conservation equations together with the k-ε *turbulence equation for the gas phase and the granular temperature equation for the solid phase. The PDF method is applied to solve the species continuity equations and avoids the need to model the chemical source terms in the latter. Stochastic differential equations (SDEs) are introduced as replicas of the transported composition PDF equations. The notional-particle-based Monte-Carlo technique is used to solve the PDF model equations. The hybrid FV/PDF solution algorithm is applied to simulate a fluid catalytic cracking (FCC) riser using a 12-lump kinetic model. A good agreement between simulated results and available plant data is obtained.* © 2011 American Institute of Chemical Engineers *AIChE J,* 58: 268–284, 2012

Keywords: gas-solid flow, stochastic differential equations, fluid catalytic cracking, micromixing, Monte-Carlo

Introduction

Fluid catalytic cracking (FCC) is one of the major industrial processes to crack heavy oil fractions into more valuable products such as gasoline and LPG. Detailed modeling of the riser reactor is a challenging task due to complexity of the turbulent reactive flow. An accurate simulation of the latter is strongly influenced by the applied turbulence models, reaction models, and numerical solution algorithms.[1] The increase of the computational capacity allows more than ever the use of computational fluid dynamics (CFD) using detailed models and reliable solution techniques.

Several studies have been reported in the open literature dealing with CFD-based modeling, simulation and kinetics in FCC risers.[2,3] All these studies neglect the effect of turbulence on the reaction source term in the Reynolds averaged species continuity equations. The latter implies that an infinitely fast mixing rate is considered for all species in the gas phase. The models implemented to describe the gas-solid hydrodynamics are of the Eulerian-Eulerian method. Typically, it is assumed that the scalars, that is, species concentrations, are uniform at the subgrid level. This assumption is justified if the time scale of reaction is considerably larger than the time scale of mixing for the implemented grid. However, in general, the subgrid species fluctuations and nonuniformities need to be accounted for by applying appropriate models.[4] A model describing a finite mixing rate must, thus, be included in the simulations.

The principle attraction of applying a transported scalar probability density function (PDF) method is that it allows to treat the highly nonlinear chemical source term in the species continuity equations without the need for closure.

Correspondence concerning this article should be addressed to G. J. Heynderickx at Geraldine.Heynderickx@UGent.be.

Closure of this chemical source term is required when conventional methods such as Reynolds averaging (RANS) or large eddy simulation (LES) are applied. Instead, the modeling challenges shift to the application of micromixing models, describing the combined effects of turbulent mixing and molecular diffusion in a transported scalar PDF.[5–7]

In this article, the transported composition PDF for gas-solid reactive flow is implemented, resulting in an in-house developed code FLOWMER-PDF. This code uses an Eulerian-Eulerian method to calculate hydrodynamic properties as described by Das et al.,[3] and a Lagrangian method to calculate species concentration fields as described by Vegendla et al.,[6] for a gas-solid flow. It continues building on a previously developed code, FLOWMER, but constitute a major step forward.[3,8–10] In the FLOWMER code, an Eulerian-Eulerian method was used. This code was validated by the simulation of two riser operations: the selective adsorption of SO_2-NO_x from stack gases[11,12] and FCC,[3] the latter being the more critical because of, in particular, the higher solids volume fraction and gas density variation. In the FLOWMER code, infinite rate mixing is assumed. As such, the turbulent fluctuations of the reaction source terms are neglected. Moreover, in the FCC case, the temperature profiles for gas and solid phase were imposed to reduce the computational cost.

In a first step, the gas-solid flow transported scalar PDF approach is validated for a constant density reactive flow situation.[6] Vegendla et al.,[6] have shown that the qualitative finite-rate mixing simulation results are more comparable with the pilot plant outlet concentrations than the simulation results obtained under infinite-rate mixing conditions, that is, conditions similar to Reynolds averaged simulations. In the constant density flow simulated by Vegendla et al.,[6] the decoupled algorithm is implemented to calculate the hydrodynamic variables and the species concentrations. This article reports on the more critical and industrially more important FCC riser operation. In this article, a coupled algorithm is implemented to be able to consider the density variations due to reactions.

Gas-solid flow model (Eulerian-Eulerian)

The time-smoothed conservation equations for the turbulent gas flow are obtained from the instantaneous equations after RANS of the total mass and momentum equations. The gas-phase turbulence is evaluated by the k-ε turbulence model[13] (see Table 1 in Das et al.[10]). This k-ε turbulence model is based on the assumption of homogeneous isotropic conditions in the turbulent flow. Solid-phase conservation equations of total mass and momentum are derived from the kinetic theory of granular flow (KTGF)[14] (see Table 2 in Das et al.[10]). The above sets of equations are completed with the required constitutive equations (see Table 3 in Das et al.[10]). For the appropriate boundary and initial conditions, reference is made to Das et al.,[3] as well. As seen in Figure 1, the hydrodynamic variables for the gas phase and solid phase are obtained by solving the partial differential equations (PDEs). The momentum exchange term is used to support the solid phase by the gas phase (i.e., to exert the drag force on the solid phase by the gas phase). As seen in Figure 1, a total of 11 PDEs needs to be solved to obtain the values for the 11 unknown variables, that is, ε_g, P, u_x, u_y, u_z, v_x, v_y, v_z, k, ε, and θ.

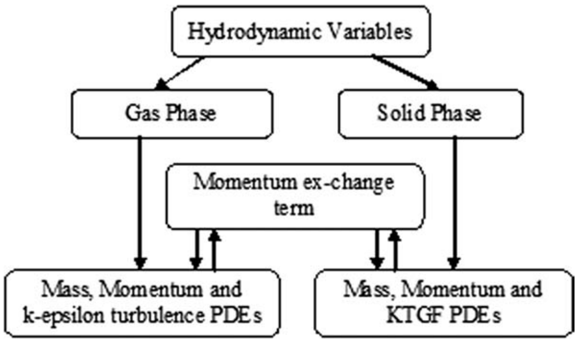

Figure 1. Calculation procedure for the flow field.

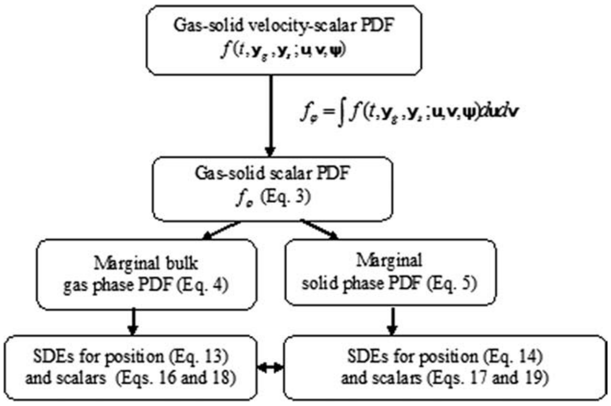

Figure 2. Calculation procedure for the scalar, that is, composition and temperature, fields.

Transported scalar PDF method

The one-point transported scalar PDF $f_\varphi(\psi;\mathbf{y},t)$ is defined as the probability of observing the event that the values of scalars φ at a time t and position $\mathbf{y}$ are found in the differential neighborhood of given values of ψ:

$$f_\varphi(\psi; \mathbf{y}, t)d\psi = P[(\psi < \varphi \leq \psi + d\psi)] \qquad (1)$$

Gas-solid species model

For a reactive, dispersed gas-solid flow, an appropriate state vector is given by:[6]

$$\boldsymbol{Z} = [\boldsymbol{y}_g, \boldsymbol{u}, \psi_g, \boldsymbol{y}_s, \boldsymbol{v}, \psi_s] \qquad (2)$$

where, $\boldsymbol{y}_g$, $\boldsymbol{y}_s$ are the position vectors of the gas and solid phase, $\boldsymbol{u}$, $\boldsymbol{v}$ are velocity vectors of the gas and solid phase and ψ_g and ψ_s are the composition vectors of the gas and solid phase, respectively.

In general, the formulation of a gas-solid transported velocity-scalar PDF is based on the above state vector (Eq. 2). Details on the velocity-scalar PDF can be found in Minier and Peirano.[15] As seen in Figure 2, a reduced form of the gas-solid transported scalar PDF is obtained by integration over the velocities of gas and solid phase.[6,16] Two marginal one-point transported scalar PDFs for the gas and the solid phase are formulated by integrating over the solid and the gas-phase species concentrations, respectively. As seen in Figure 2, these marginal one-point transported scalar PDFs for the gas phase and the solid phase are modeled in terms of stochastic differential equations (SDEs), solved for position and composition updates. More details for the formulations of the transported scalar PDFs and their modeling details are discussed in the following paragraphs.

Transported scalar PDF equations for the FCC process are formulated based on the gas-solid (FCC) reactive species continuity equations.[3,16] Species continuity equations are considered for the bulk gas phase and for the coke surface species in the solid phase, that is, on the catalyst particles. The energy balance equations for the gas phase and solid phase are also considered. Both external mass and heat transfer, that is, transfer between the gas phase, and the external surface of the catalyst particles is considered explicitly in the model equations. Species concentration and temperature gradients inside the catalyst particles are neglected. The heat flux across the wall is considered to be zero. Heat production or dissipation due to catalyst particle–particle and catalyst particle-wall collisions are not included in the modeled equations.

An equation for the transported scalar distribution function for gas-solid flow is formulated based on the work of Minier and Peirano,[15] Carrara and DesJardin,[17,18] and Vegendla et al.[6] It is an extension of the one-point transported scalar PDF equation in single-phase gas flow [7] and is referred to as a joint two-point (one-point for gas and one-point for solid phase) transported scalar distribution function equation:

$$\frac{\partial(f_\varphi)}{\partial t}+\tilde{\mathbf{u}}\frac{\partial(f_\varphi)}{\partial \boldsymbol{y}_{\mathrm{g}}}+\tilde{\mathbf{v}}\frac{\partial(f_\varphi)}{\partial \boldsymbol{y}_{\mathrm{s}}}+\frac{\partial}{\partial \boldsymbol{y}_{\mathrm{g}}}\left[\langle \mathbf{u}''|\mathbf{Z}=z\rangle f_\varphi\right]$$
$$+\frac{\partial}{\partial \boldsymbol{y}_{\mathrm{s}}}\left[\langle \mathbf{v}''|\mathbf{Z}=z\rangle f_\varphi\right]=-\frac{\partial}{\partial \psi_{\alpha\mathrm{g}}}\begin{bmatrix}\langle D_{\alpha\mathrm{g}}\nabla^2\phi_{\alpha\mathrm{g}}|\mathbf{Z}=z\rangle f_\varphi\\ +S_{\mathrm{gs}}(\psi)f_\varphi\end{bmatrix}$$
$$-\frac{\partial}{\partial \psi_{\alpha\mathrm{gs}}}\begin{bmatrix}-S_{\mathrm{gs}}(\psi)f_\varphi\\ +R_{\alpha\mathrm{gs}}(\psi)f_\varphi\end{bmatrix}-\frac{\partial}{\partial \psi_{\alpha\mathrm{s}}}\left[R_{\alpha\mathrm{s}}(\psi)f_\varphi\right] \tag{3}$$

where $< >$ represents the ensemble average, based on a specified number of samples.

The first term on the left hand side (LHS) represents the rate of change of the composition PDF, the second term represents the gas-phase convection, the third term represents the solid-phase convection, the fourth term represents the gas-phase velocity fluctuation, and the fifth term represents the solid-phase velocity fluctuation.

The first term in the right hand side (RHS) represents the conditional scalar fluctuation and mass transfer or heat transfer in the bulk gas phase. The second term represents the mass transfer or heat transfer and the reaction source in the solid phase for gas species, and the third term represents the species adsorbed on the solid surface.

Two marginal one-point composition PDFs are derived from the basic two-point composition PDF for the reactive gas-solid flow (Eq. 3). These marginal PDFs are comparable to the one-point composition PDF for single-phase gas flow. The first marginal equation represents the gas species in the bulk gas phase (Eq. 4), and the second marginal equation represents the gas species and surface species in the solid phase (Eq. 5).

The marginal one-point transported scalar PDF $f_{\varphi_{\mathrm{g}}}$ for the bulk gas-phase species including temperature (see below) follows from

$$\frac{\partial(\rho_{\mathrm{g}}f_{\varphi_{\mathrm{g}}})}{\partial t}+\tilde{u}\frac{\partial(\rho_{\mathrm{g}}f_{\varphi_{\mathrm{g}}})}{\partial \boldsymbol{y}_{\mathbf{g}}}+\frac{\partial}{\partial \boldsymbol{y}_{\mathbf{g}}}\left[\langle \mathbf{u}''|\psi\rangle \rho_{\mathrm{g}}f_{\varphi_{\mathrm{g}}}\right]$$
$$=-\frac{\partial}{\partial \psi_{\alpha\mathrm{g}}}\left[\left(\langle D_{\alpha\mathrm{g}}\nabla^2\phi_{\alpha\mathrm{g}}|\psi\rangle+S_{\mathrm{gs}}(\psi)\right)\rho_{\mathrm{g}}f_{\varphi_{\mathrm{g}}}\right] \tag{4}$$

The marginal one-point transported scalar PDF $f_{\varphi_{\mathrm{s}}}$ for the surface species including temperature (see below) in the solid phase follows from

$$\frac{\partial(\rho_{\mathrm{sp}}f_{\varphi_{\mathrm{s}}})}{\partial t}+\tilde{v}\frac{\partial(\rho_{\mathrm{sp}}f_{\varphi_{\mathrm{s}}})}{\partial \boldsymbol{y}_{\mathbf{s}}}+\frac{\partial}{\partial \boldsymbol{y}_{\mathbf{s}}}\left[\langle \mathbf{v}''|\psi\rangle \rho_{\mathrm{sp}}f_{\varphi_{\mathrm{s}}}\right]$$
$$=-\frac{\partial}{\partial \psi_{\alpha\mathrm{s}}}\left[-S_{\mathrm{gs}}(\psi)\rho_{\mathrm{sp}}f_{\varphi_{\mathrm{s}}}+R_{\alpha\mathrm{s}}(\psi)\rho_{\mathrm{sp}}f_{\varphi_{\mathrm{s}}}\right] \tag{5}$$

The mass-transfer term from the bulk gas phase to the solid phase is given by

$$S_{\mathrm{gs}}(\psi)=k_{\mathrm{g_s}}(a_{\mathrm{m}}\varepsilon_{\mathrm{s}}\rho_{\mathrm{sp}})\left(\frac{RT}{P}\right)(\varphi_{\mathrm{gs}}-\varphi_{\mathrm{g}}) \tag{6}$$

Closure terms for gas-solid flows

In the marginal one-point transported scalar PDF equation for the bulk gas phase, the scalar-conditioned velocity fluctuation mesomixing term (third term in LHS of Eq. 4) is closed using a gradient-diffusion model[7,19]

$$\langle \mathbf{u}''|\psi\rangle \rho_{\mathrm{g}}f_{\varphi_{\mathrm{g}}}=-\frac{\mu_{\mathrm{g}}^{\mathrm{t}}}{<\rho_{\mathrm{g}}>Sc_{\mathrm{g}}^{\mathrm{t}}}\frac{\partial(\rho_{\mathrm{g}}f_{\varphi_{\mathrm{g}}})}{\partial \boldsymbol{y}_{\mathrm{g}}} \tag{7}$$

Mesomixing is defined as convective transport arising from the scalar-conditioned velocity fluctuations in the riser reactor. Mesomixing is due to the breaking-down of volume elements in the reactor due to large eddies.

For the solid phase, the scalar-conditioned velocity fluctuation term is modeled in a similar way (third term in LHS of Eq. 5):

$$\langle \mathbf{v}''|\psi\rangle \rho_{\mathrm{sp}}f_{\varphi_{\mathrm{s}}}=-\frac{\mu_{\mathrm{s}}}{<\rho_{\mathrm{sp}}>Sc_{\mathrm{s}}^{\mathrm{t}}}\frac{\partial(\rho_{\mathrm{sp}}f_{\varphi_{\mathrm{s}}})}{\partial \boldsymbol{y}_{\mathrm{s}}} \tag{8}$$

The scalar-conditioned micromixing term (first term in RHS of Eq. 4) is closed using the interaction-by-exchange-with-mean (IEM) model:[7,19,20]

$$\langle D_{\mathrm{g}}\nabla^2\varphi_{\mathrm{g}}|\psi\rangle=\frac{1}{\tau_\phi}(<\varphi_{\mathrm{g}}(\mathbf{y},t)>-\psi_{\alpha\mathrm{g}}) \tag{9}$$

where $<\varphi_{\mathrm{g}}(\boldsymbol{y},t)>$ is the mean value of the local scalar at the position $\boldsymbol{y}$ and time t and τ_ϕ is the local micromixing time, calculated as:[21]

$$C_\phi \tau_\phi \cong \frac{k}{\varepsilon} \cong \tau_u \tag{10}$$

where C_ϕ is the mechanical-to-scalar time-scale ratio, a parameter of the IEM model.

Micromixing is defined as mixing at the smallest length scale in the riser reactor. This length scale corresponds to that of the small eddies in the riser reactor. The phenomenon of micromixing can be considered similar to the phenomenon of molecular mixing.

Source terms such as reaction rates appear in closed form in both marginal one-point transported scalar PDF equations (Eqs. 4 and 5).

Solution procedure

All computational results presented in this work are obtained with the in-house developed CFD code FLOWMER-PDF. Figure 3, gives an overview of the various steps involved in an one-point marginal transported PDFs simulation using the in-house FLOWMER-PDF code. This code solves the set of partial differential equations (PDEs) for the conservation of total mass and momentum for the gas phase and the solid phase, together with the k-ε turbulence model equations for the gas phase, the granular temperature equation for the solid phase (KTGF) (Figure 1).[10] By solving this set of equations, the hydrodynamic properties of the FCC riser reactor are evaluated. The obtained flow information is used when solving the marginal one-point transported scalar PDF equations (Figure 2).

To solve the flow PDEs for the gas phase and the solid phase, a dual time step procedure and density-based algorithm is implemented.[8,9] The following descretization techniques are used in the present simulations to calculate the gas and solid flow fields. The time derivatives are discretized using a first-order Euler backward scheme. The convection fluxes are discretized using the advective upwind splitting method. The pressure terms are discretized using a central scheme. Finally, the viscous terms and the source terms are linearized as discussed in De Wilde et al.[8,9]

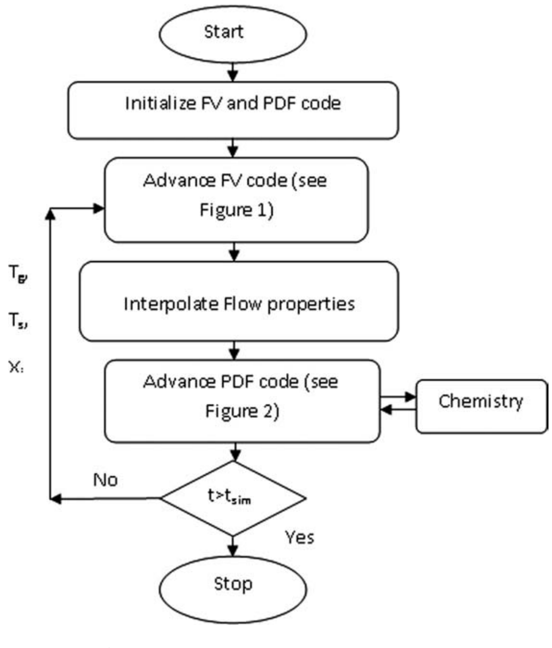

Figure 3. Simulation procedure for reactive flows.

Notional-particle method

Solving the marginal one-point transported scalar PDF equations, using standard solution techniques such as finite volume (FV) and finite difference (FD), is computationally prohibitive for a large number of independent variables (e.g., the position vector and the number of species). Therefore, a Monte-Carlo (MC) particle-mesh technique is implemented. The marginal one-point transported scalar PDF equations are modeled in terms of SDEs to calculate position and composition updates as discussed above (Figure 2). To replicate the PDF solution using modeled the SDEs, a large number of so-called notional particles, randomly and continuously distributed over the flow domain,[5] is needed. The notional particles must be considered as surrogate particles for the solid catalyst particles or for the fluid elements. The position of these notional particles in physical space (Eqs. 13 and 14) and the corresponding scalars (Eqs. 16–19) are determined by solving a set of SDEs. The SDEs for the notional particles are the replicas of the transported scalar PDF equations.

The transported composition PDFs (Eqs. 4 and 5) need to be solved for a large number of notional particles that covers the entire computational domain of the FCC riser reactor to obtain an accurate estimate of the mean, $\langle \varphi \rangle$, and variance, φ_{var}, composition fields by averaging out over all notional particles in the given cell

$$\langle \varphi_l \rangle = \frac{\sum_{n=1}^{N_l} m_l^n \varphi_l^n}{\sum_{n=1}^{N_l} m_l^n} \tag{11}$$

where, m_l^n is the mass of notional-particle, and φ_l^n is the chemical composition vector for the nth particle in a given mesh cell “l”

$$\varphi_{\text{var}} = \sqrt{\frac{1}{N_l - 1} \sum_{n=1}^{N_l} \left[\varphi_l^n - <\varphi_l>\right]^2} \tag{12}$$

In single-phase gas flow, one set of notional particles suffices.[7] However, two different sets of notional particles are required to solve the two marginal one-point transported scalar PDF equations (Eqs. 4 and 5) for the gas-solid FCC riser reactor; one set for the bulk gas phase (Eq. 4) and one set for the solid phase (Eq. 5).

First, the notional particles representing the gas phase and the solid phase are uniformly distributed over the riser grid and assigned a composition and temperature. Next, the total mass of gas and solid notional particles are initialized, based on the mass of the gas and the solid in a given cell. To control the particle number density in a given cell, the notional particles are combined or split, using a cluster or clone algorithm in a grid cell.[5] This approach helps to reduce statistical errors when calculating mean scalar quantities.

The SDE to determine the position of the bulk gas-phase notional particle (Eq. 13) is obtained from Eq. 4, as discussed in Kolhapure et al.,[7] for single-phase gas flow. A comparable

SDE (Eq. 14) obtained from Eq. 5, is used to determine the position of the notional particle for the solid phase (Eq. 5):

$$d\mathbf{y}^{\mathrm{ng}} = \left(\tilde{\mathbf{u}} + \frac{\nabla(\mu_{\mathrm{g}} + \mu_{\mathrm{g}}^{\mathrm{t}})}{<\rho_{\mathrm{g}}>}\right)dt + \sqrt{2\frac{(\mu_{\mathrm{g}} + \mu_{\mathrm{g}}^{\mathrm{t}})}{<\rho_{\mathrm{g}}>}}\, d\mathbf{W} \qquad (13)$$

and

$$d\mathbf{y}^{\mathrm{ns}} = \left(\tilde{\mathbf{v}} + \frac{\nabla(\mu_{\mathrm{s}})}{<\rho_{\mathrm{s}}>}\right)dt + \sqrt{2\frac{(\mu_{\mathrm{s}})}{<\rho_{\mathrm{s}}>}}\, d\mathbf{W} \qquad (14)$$

$$d\mathbf{W} = \xi\sqrt{dt} \qquad (15)$$

The first term in the RHS of Eq. 13 represents the convection arising from the mean velocity, the molecular and the turbulent diffusivity of the bulk gas phase. The first term in the RHS of Eq. 14, represents the convection arising from the mean velocity, the collisional, and the kinetic diffusivity of the solid phase. The last term in Eqs. 13 and 14 represents the Wiener-diffusion process (*dW*) characterized by a Gaussian process with zero mean and variance *dt*.[5] Solving the Eqs. 13 and 14, for every notional-particle provides their location as a function of time.

The SDE to determine the composition of a notional particle in the bulk gas phase, Eq. 16 is obtained from Eq. 4, as discussed in Kolhapure et al.,[7] for single-phase gas flow. A comparable SDE (Eq. 17) obtained from Eq. 5 is used to determine the composition of the notional particle for the surface species:[6]

No distinction is made between the species concentration in the bulk gas phase and the gas phase inside the pores of the solid particles. This is due to the high-rate of mass transfer between the gas and the solid phase.

The SDE for the gas-phase notional-particle[6] is:

$$d\varphi_{\mathrm{g}}^{\mathrm{ng}} = \left(\frac{C_\phi}{2\tau_\phi}\left(<\varphi_{\mathrm{g}}> - \varphi_{\mathrm{g}}^{\mathrm{ng}}\right) + \frac{r_{\mathrm{g}}(1-\varepsilon_{\mathrm{g}})\rho_{\mathrm{s}}}{\varepsilon_{\mathrm{g}}}\right)dt \qquad (16)$$

The SDE for the solid-phase notional-particle[6] is:

$$d\varphi_{\mathrm{s}}^{\mathrm{ns}} = R_{\mathrm{s}}dt \qquad (17)$$

The SDE to determine the gas-phase notional-particle temperature:

$$dT_{\mathrm{g}}^{\mathrm{ng}} = \left(\frac{C_\phi}{2\tau_\phi}\left(<T_{\mathrm{g}}> - T_{\mathrm{g}}^{\mathrm{ng}} + \frac{h_{\mathrm{gs}}a_{\mathrm{m}}(1-\varepsilon_{\mathrm{g}})\rho_{\mathrm{p}}}{C_{\mathrm{g}}\varepsilon_{\mathrm{g}}\rho_{\mathrm{g}}}\left(<T_{\mathrm{s}}|\mathbf{y}_{\mathrm{g}}> - T_{\mathrm{g}}^{\mathrm{ng}}\right)\right)\right)dt \qquad (18)$$

and, the SDE for solid-phase notional-particle temperature:

$$dT_{\mathrm{s}}^{\mathrm{ns}} = \left(\frac{h_{\mathrm{gs}}a_{\mathrm{m}}}{C_{\mathrm{p}}}\left(<T_{\mathrm{g}}|\mathbf{y}_{\mathrm{s}}> - T_{\mathrm{s}}^{\mathrm{ns}}\right) + \frac{\Delta H_{\mathrm{rxn}}}{C_{\mathrm{p}}}\right)dt \qquad (19)$$

The terms in the RHS of Eq. 16 represent the micromixing term and the reaction term in composition space. The term in the RHS of Eq. 17 represents the reaction source term in composition space determining the coke content of the solid phase.

In addition, SDEs for calculating temperature of the gas and solid phase are formulated (Eqs. 18 and 19). They correspond to Eqs. 16 and 17. The first term in the RHS of Eq. 18 represents the micromixing and the second term represents heat transfer between the gas phase and the solid phase. The first term in the RHS of Eq. 19 represents the heat transfer between the gas phase and the solid phase and the second term represents the heat of reaction.

Solving the Eqs. 16 to 19 for every notional-particle provides their composition and temperature as a function of time.

Particle tracking

The MC numerical solution technique for the transported scalar PDF equations demands a Lagrangian–Eulerian approach. Each notional particle has to be associated with a grid cell in the computational domain. Lagrangian tracking of the notional particles is done in three steps: (1) determine the grid cell a notional particle is located in, (2) interpolate the field variables at the notional-particle location, and (3) update the position of the particle according to the velocity vector and the turbulent diffusivity within the gas phase and the solid phase (Eqs. 13 and 14) using a time integration method. Boundary conditions (BC) for the notional-particle tracking procedure are taken from Fox.[5]

Search algorithm for notional particles

In the first step, the position of the notional particles is to be determined. Three possible algorithms are available: the brute-force algorithm, the modified brute-force algorithm, and the known-vicinity search algorithm, as reported by Apte et al.[22]

In FLOWMER-PDF, the modified brute-force algorithm is implemented. This algorithm determines the mesh point closest to the notional-particle location and only considers the grid cells that surround this mesh point. The algorithm can take two approaches, as described below. The first approach to determine whether a particle is situated in a given grid cell, is based on the calculation of partial volumes. The nodes of the grid cell under consideration are linked to the particle location, and the volumes of the resulting subcells are summed up and compared to the total volume of the grid cell. If the particle is indeed situated in the given grid cell, the sum of the subcell volumes will be equal to the total volume of the given control volume (grid cell). However, this approach is found to fail drastically for highly skewed meshes (as obtained for complicated geometries like Diesel engine) due to round-off inaccuracies in the computation of the partial volumes. The second approach is the face-to-face strategy. This strategy projects the notional-particle location onto the faces of the grid cell under consideration and compares the obtained vectors with the outward face-normals for all faces of the grid cell. If the particle is positioned within the grid cell, the projected vectors point the same way as the outward face-normals. This technique is found to be very accurate, even for highly skewed meshes. Considering both approaches, the face-to-face strategy has proven to be the most promising tool.[22,23]

Interpolation of the gas-solid variables to the notional-particle location

In the second step, the flow variables must be interpolated to obtain their values in the notional-particle location as determined in Step 1. In practice, the grids used in many CFD applications are not Cartesian. To handle complex geometries such as the riser reactor (FCC), curvilinear grids are used. Such grids are also referred to as structured grids, because they have a regular topological structure, as opposed to unstructured grids. The information on the gas and solid properties obtained by solving the flow model equations (see Tables 1–3 in Das et al.[10]) using the FV technique is available at the center of each grid cell. Several schemes can be used to interpolate these flow properties to the notional-particle location.[24] A trilinear interpolation scheme with an inverse distance-weighing algorithm is implemented for the curvilinear grid used in the in-house developed code FLOWMER-PDF. The inverse distance weighing technique is explained next.

Let $\mathbf{y}_1 \ldots to \ldots\ldots \mathbf{y}_\mathrm{k}$ be the coordinates of the k corner nodes of a particular grid cell (hexa, tetra, etc.) volume, and let $\mathbf{u}_1 \ldots to \ldots\ldots \mathbf{u}_\mathrm{k}$ be the velocities in those nodes. The latter follow from the flow properties at cell corners obtained from neighboring cell center values by averaging. Then, the interpolated velocity ($\mathbf{u}$) value at the notional-particle location ($\mathbf{Y}_\mathrm{i}$) is calculated as a weighted average of the corner values.

$$\mathbf{u} = \mathbf{w}_1\mathbf{u}_1 + \ldots\ldots + \mathbf{w}_k\mathbf{u}_\mathrm{k} \tag{20}$$

The weight of each contribution is calculated as a function of the Euclidian distance between the corner node $\mathbf{y}_\mathrm{i}$ and notional-particle position $\mathbf{Y}_\mathrm{i}$:

$$\mathrm{d}_i = \left\| \mathbf{y}_\mathrm{i} - \mathbf{Y}_i \right\| \tag{21}$$

$$\mathbf{w}_i = \frac{\frac{1}{d_i^2}}{\sum_{j=1}^{k} \frac{1}{d_j^2}} \tag{22}$$

If $\mathbf{Y}_\mathrm{i}$ is close to a corner node, the distance d_i will be nearly zero, and the interpolated value becomes unpredictable when using Eq. 22. This is handled in the algorithm by testing whether the distance d_i is close to zero. If so, the weight of that corner node is taken equal to one, whereas the weight of all other nodes is set equal to zero. The advantage of the inverse distance weighing technique is that it does not require the fractional offset as used in the stencil walk/Newton-Raphson iteration.[24]

Update notional-particle location

In the third and last step, the position of the notional particle is updated using the simplest numerical method to integrate the notional-particle position SDEs (Eqs. 13 and 14), that is the explicit forward Euler scheme, in which the solution is advanced from time t_o to time $t_\mathrm{o} + \Delta t$.

Boundary conditions for notional-particle tracking

During the MC simulations, BC must be applied at the edge of the physical simulation domain. The four most common types of BC are inflow, outflow, symmetry, and zero-flux wall BC. For the FCC simulations, symmetry cannot be considered. The procedure for inflow, outflow, and zero-flux wall BC is considered, implemented as explained in Fox.[5]

Computational cost

The flow equations are integrated in a steady-state mode, that is, using an infinite physical time step. The total amount of CPU time for one iteration is around 4 min on Xeon processor having 1.4 GHz and 1 GB RAM on a linux operating system 9.0.

Composition PDF methods are computationally expensive when compared with FV reactor model simulations. This is due to the lower number of equations that are needed to be solved when using a FV reactor model as compared to using a composition PDF method. In the given riser geometry, the total number of grid cells considered is 12,931 using 20 notional particles for the gas phase and 20 notional particles for the solid phase in each cell. In this work, a 3D grid is generated using an in-house developed code by De Wilde et al.[8,9] In this 3D geometry, a total of 67 horizontal planes are considered along the riser height with 193 grid points in each of these planes. The CPU time required to follow the above mentioned number of notional particles over the entire geometry of the riser for one time step, that is, physical time step of 0.005 s, is about 4.5 min on a single 1.4 GHz Xeon processor and 1 GB RAM (linux operating system 9.0).

As seen in Figure 3, the FV simulations are performed following the initialization of the flow and reaction variables. Next, the resulting flow variable information is used to progress the PDF code. The flow variables are stored at the cell centers during the FV simulations as described above. To progress the PDF code, these cell center flow values need to be interpolated to the notional particles location in each grid cell. This is done by using a tri-linear inverse distance weighting method. Based on the flow information, the PDF code updates the notional particles information for positions in physical space and species concentrations in compositions space. The obtained species concentrations and temperatures are the used as an input for the FV code. In the hybrid FV-PDF algorithm, this forward and backward updating of information is continued until convergence is reached.

Initially, a decoupled hybrid solution algorithm is used for flow and reaction to reduce the initialization errors. Later, a coupled hybrid solution algorithm is implemented with 10 iterations of flow followed by two iteration of reaction until convergence is achieved. As seen in Figure 4, the total amount of CPU time required to reach a statistically stationary solution is around 120 days on a single processor. As seen in Figure 4, the total residuals drop by three orders of magnitude for flow and two orders of magnitude for reaction. The required CPU time will increase linearly with the number of notional particles followed and the number of time steps taken. As discussed above, solving the marginal composition PDFs using conventional techniques like FV and FD is computationally prohibitive. Nevertheless, the use of a MC simulation technique requires more CPU time as the number of notional particles in the reactor increases.

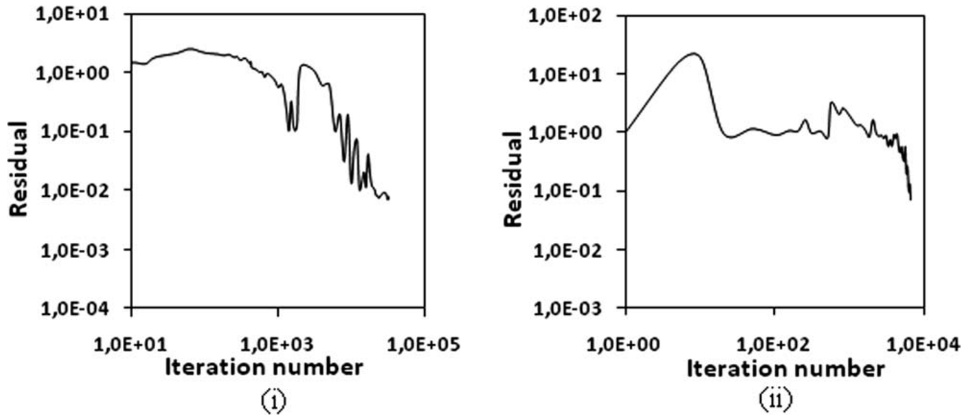

Figure 4. Log–Log plot of normalized residuals versus. iteration number for (a) flow and (b) reaction, for a finite-rate mixing (C_φ = 1).

Operating conditions: see Table 1.

Consistency

The newly developed hybrid algorithm is consistent at the level of the modeled equation.[1] To solve the above mentioned modeling equations numerically can produce inconsistencies. To achieve the consistency and enhance the stability between the FV and the PDF code, time averaging is performed, ($<\varphi^{i+1}> = (1 - N_{\mathrm{TA}}^{-1}) <\varphi^{i}> + N_{\mathrm{TA}}^{-1}<\varphi^{i+1}>$), once the statistically stationary state is reached (a N_{TA} of 1,000 is used). As seen in Figure 5, there is a small difference between the mean density calculated using the FV code and using the hybrid PDF code, at a riser height of 4 m. This deviation could be a consequence of the applied solution technique. In the hybrid algorithm flow variables are obtained using the Eulerian method. Reaction species concentrations are obtained using Lagrangian method.

FCC pilot plant riser reactor

The riser geometry and operating conditions are presented in Table 1 for the FCC riser simulation. The 12-lump kinetic model for the FCC reactions used in this work is based on the work of Peixoto and Medeiros.[25] The detailed mechanism of the reactions and stoichiometry are discussed in Peixoto and Medeiros.[25] As seen in Table 1, the introduced scalar feed at the inlet cannot be considered as either non-premixed or premixed due to the differences in the gas and the solid phase temperatures.

The reaction time scales vary from 10^{-2} to 10^{-1} s. For mixing, external mass transfer, heat transfer, and intraparticle diffusion, time scales of the order of 10^{-3} to 10^{-1}, 10^{-4}, 10^{-3} to 10^{-4}, and 10^{-5} s, respectively, are obtained. The FCC reactor is thus mixing and reaction controlled. There is no need to account for external mass transfer. The small time scale for intraparticle diffusion allows to assume uniformity inside the catalyst particles. The intracrystallite diffusion is neglected in the presented work.

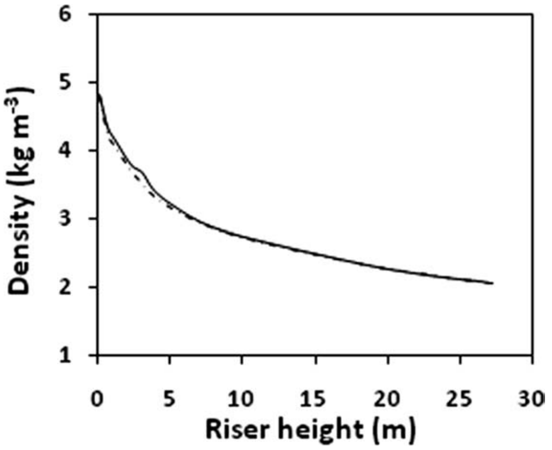

Figure 5. Comparison of the radially averaged gas density along the length of the riser in FV code (dashed line) and PDF code (solid line), for a finite-rate mixing (C_φ = 1).

Operating conditions: see Table 1.

Table 1. FCC Riser Dimensions and Operating Conditions Used in the Simulation[2,3]

Property/Parameter	Units	Case 1
Riser height	m	27.35
Riser diameter	m	0.4
Outlet elevation	m	26.83
Total outlet surface area	m^2	0.16
Particle diameter	μm	65
Particle density	kg m^{-3}	1500
Restitution coefficient	–	1.0
Wall restitution coefficient	–	0.9
Inlet		
Solid volume fraction	–	0.0816
Solid flux	kg m^{-2} s^{-1}	79.0
Average gas velocity	m s^{-1}	4.55
Granular temperature	m^2 s^{-2}	0.14
Gas turbulent intensity	–	0.02
Feed temperature	K	698
Catalyst temperature	K	875
Feed mass flow rate	kg s^{-1}	2.68
Steam mass flow rate	kg s^{-1}	0.047
Feed composition	wt. fraction	
P_h		0.67
N_h		0.0918
A_h		0.1736
F_h		0.0616
Steam		0.26
Outlet pressure	10^5 Pa	1.013

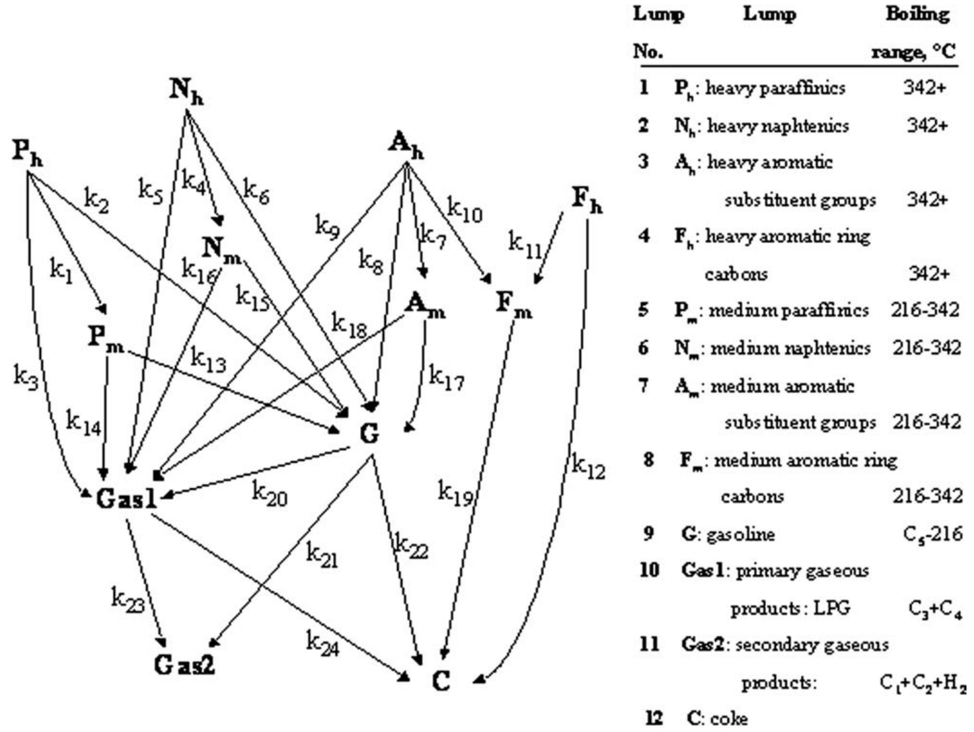

Lump No.	Lump	Boiling range, °C
1	**P_h**: heavy paraffinics	342+
2	**N_h**: heavy naphtenics	342+
3	**A_h**: heavy aromatic substituent groups	342+
4	**F_h**: heavy aromatic ring carbons	342+
5	**P_m**: medium paraffinics	216-342
6	**N_m**: medium naphtenics	216-342
7	**A_m**: medium aromatic substituent groups	216-342
8	**F_m**: medium aromatic ring carbons	216-342
9	**G**: gasoline	C_5-216
10	**Gas1**: primary gaseous products: LPG	C_3+C_4
11	**Gas2**: secondary gaseous products:	$C_1+C_2+H_2$
12	**C**: coke	

Figure 6. Reaction network of the 12-lump FCC kinetic model.[25]

In this paper, the gas-solid flow fields are calculated by solving a total of 11 PDEs for 11 unknown variables, that is, ε_g, P, u_x, u_y, u_z, v_x, v_y, v_z, k, ε, and θ. On the other hand, for the gas-solid reactions, a total of 21 modeled SDEs has to be solved for each notional particle to calculate the temperature of both phases, the position vector for both phases, and the gas species and cokes (solid phase) concentrations.

Kinetic model

As discussed above the 12-lump kinetic model proposed by Peixoto and Medeiros[25] is adopted in this work. The 12-lump kinetic model is shown in Figure 6, while the rate coefficients and physical properties are summarised in Table 2. The stoichiometric factor of a lump j in path p can be generally expressed as:

$$\gamma_{jp} = \delta_{ij} \frac{M_i}{M_j} \tag{23}$$

where i is the reactant lump number in path p, M is the molecular mass of the lump and $\delta_{ij} = 0$ if path p is not linked to lump j (Figure 6); $\delta_{ij} = 1$ if $j > i$ and $\delta_{ij} = -1$ if $j = i$.

The deposition of coke on the catalyst surface significantly decreases the catalyst activity. The catalyst activity is related to the coke content, that is, mass fraction of coke on the catalyst C_C in accordance to the equation proposed by Gao et al.,[2] as follows:

$$\varphi_c = (1 + 51.0\, C_C)^{-2.78} \tag{24}$$

Table 2. Properties of FCC Lumps

Lump No.	Lump	Approximate Formula	Molecular Mass (kg mol^{-1})	Standard Heat of Formation, 10^5 (J mol^{-1})	Thermal Conductivity (W m^{-1} K^{-1})	Diffusion Volume (cm^3 mol^{-1})	Specific Heat Constants (J mol^{-1} K^{-1}) A	B
1	P_h	$C_{26}H_{54}$	0.3667	−7.18	0.132	535.9	402.0	1.025
2	N_h	$C_{26}H_{52}$	0.3667	−6.65	0.132	531.9	402.0	1.025
3	A_h	$C_{26}H_{54}$	0.3667	−7.18	0.132	535.9	402.0	1.025
4	F_h	$C_{26}H_{22}$	0.3384	3.57	0.132	452.3	518.4	0.27
5	P_m	$C_{18}H_{38}$	0.254	−4.14	0.12	372.2	281.2	0.71
6	N_m	$C_{18}H_{36}$	0.252	−3.76	0.12	368.3	281.2	0.71
7	A_m	$C_{18}H_{38}$	0.254	−4.14	0.12	372.2	281.2	0.71
8	F_m	$C_{18}H_{18}$	0.234	1.63	0.12	212.4	227.2	0.45
9	G	C_9H_{12}	0.126241	−0.38	0.1	152.0	123.7	0.25
10	G_1	$C_{3.5}H_9$	0.057116	0.083	0.08	71.6	56.9	0.12
11	G_2	$C_{1.5}H_{4.5}$	0.02356	−0.33	0.06	33.66	8.29	0.1
12	Coke	$C_{18}H_{18}$	0.28228	0.43	26.0	–	436.0	0.27
Steam	–	H_2O	0.018	−2.42	0.10	12.7	32.24	0.002

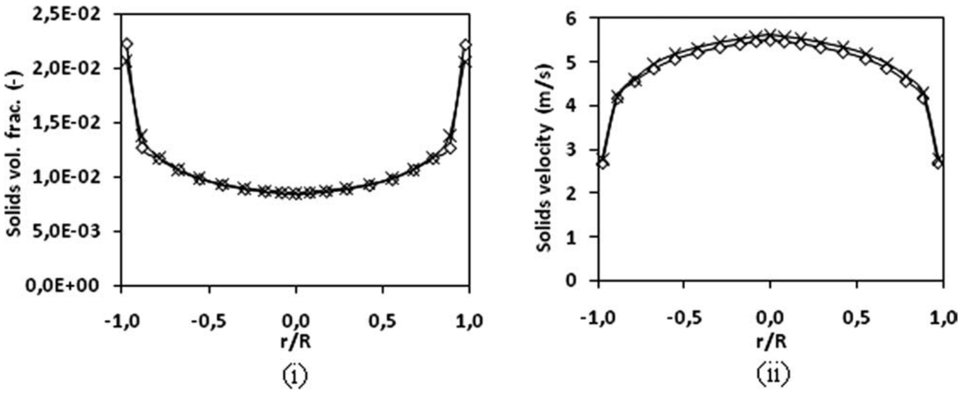

Figure 7. Radial profiles along *XZ*-plane at 0.5 m riser height for varying number of grid cells for finite-rate mixing (C_Φ = 1), (a) solids volume fraction and (b) solids velocity, (Symbols: ◇ - 965; × - 1930), using 20 notional particles and 0.005 s time step (see equations in Tables 1 to 3 in Das et al.[10]).

Operating conditions: see Table 1.

Following the kinetic scheme shown in Figure 6, it is possible to express the net production rate of a lump j based on the reaction rate of the individual steps

$$R_j = \sum_{p=1}^{m} \gamma_{jp}\, r_p \tag{25}$$

where m is the total number of reaction paths. The individual reaction rate r_p is a function of species concentration and catalyst activity

$$r_\mathrm{p} = k_\mathrm{p} e^{-\frac{E}{R}\left[\frac{1}{T}-\frac{1}{T_\mathrm{b}}\right]} \varphi_{F_\mathrm{h}} \varphi_\mathrm{c} C_\mathrm{p} \tag{26}$$

where C_p is the concentration of the reactant lump in path p in the gas phase; k_p is the rate coefficient for path p at a base temperature T_b. The factor φ_{F_h} accounts for the change in the free site concentration due to the adsorption of heavy aromatic rings F_h on the catalyst surface. Assuming the adsorption to be in equilibrium:[16]

$$\varphi_{F_\mathrm{h}} = \frac{1}{1 + K_\mathrm{h} C^\mathrm{s}_{F_\mathrm{h}}} \tag{27}$$

where K_h is the equilibrium adsorption coefficient of lump F_h.

Investigation of grid, notional-particle, and time-step dependency

In this section, the simulation results dependency on a varying number of grid cells, a varying number of notional particles, and a change in the applied time step has been evaluated.[26,27] Before simulating a full-scale riser, these effects have been evaluated on a small-scale riser with a height and a diameter of 0.5 and 0.4 m, respectively. This small-scale riser is considered to study the effect of using varying grid dimensions and a varying number of notional particles in each grid cell for a finite-rate mixing ($C_\Phi = 1$), to limit the computational time. Two types of grid with a total of 965 and 1930 cells are considered to perform simulations for a different number of notional particles of 10, 20, 50, and 100, in the 3D geometry of the small-scale riser reactor.

As seen in Figure 7, the volume fraction and the velocity of the solids are qualitatively and quantitatively similar for both the grids cells. Further calculating by using a different number of notional particles, simulating 965 grid cells are good enough to validate the simulation results.

The mixture fraction is a nondimensional quantity representing the mass fraction of species, at a particular location. It is calculated based on the carbon-containing species, which is defined by[28]

$$\xi = X_\mathrm{h} + X_\mathrm{m}\frac{M_\mathrm{h}}{\upsilon M_\mathrm{m}} + X_\mathrm{G}\frac{M_\mathrm{h}}{\upsilon M_\mathrm{G}} + X_\mathrm{L}\frac{M_\mathrm{h}}{\upsilon M_\mathrm{L}} + X_\mathrm{c}\frac{M_\mathrm{h}}{\upsilon M_\mathrm{c}} \tag{28}$$

where ξ is the mixture fraction, X is the mass fraction, υ is the carbon number of heavy gas oil, and M is the molecular mass of the component.

The dependence of the mixture fraction and its variance on the number of notional particles used in a grid cell is presented for a finite-rate mixing ($C_\Phi = 1$) in Figure 8. The simulated mixture fraction deviates slightly, when comparing 10 notional particles with one of the 20, 50, and 100 notional particles in each grid cell. On the other hand, no differences were found in yields when using a 20, 50, and 100 notional particles (see Figure 8). As seen in Figure 8, the differences in the variances are high when using 10 notional particles when compared with the use of 20, 50, or 100 notional particles in each grid cell. On the other hand, the differences are negligible for the 20, 50, and 100 notional particles simulation results.

As seen in Figure 9, the mixture fraction and its variance are presented for considering different time steps using 20 notional particles in each grid cell for a finite-rate mixing ($C_\Phi = 1$). The differences are observed to be negligible when comparing results of mixture fraction for a different time steps (0.001 and 0.005 s). As seen in Figure 9a, the slight difference in the variances is possibly due to the change of the notional particles position. However, the overall radially averaged value is the same in both the time step results as seen in Figure 9b.

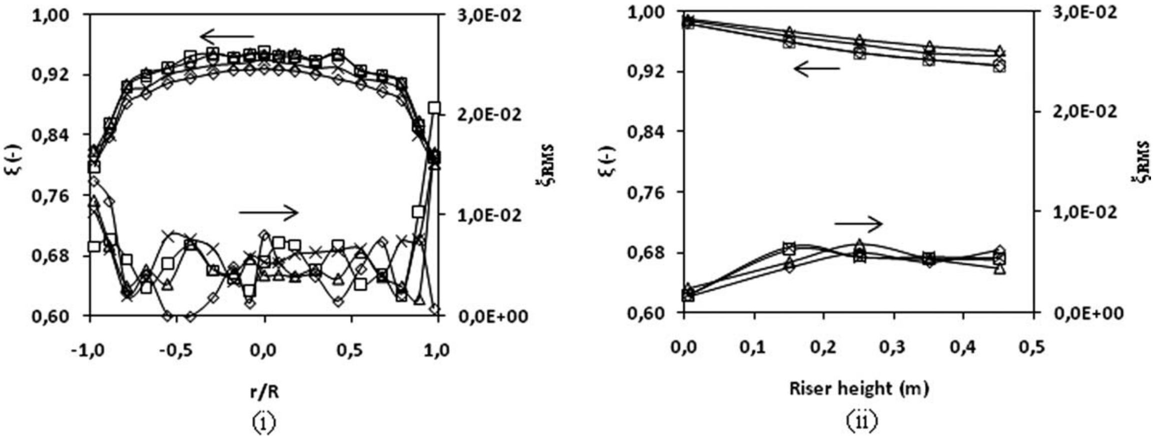

Figure 8. Heavy gas oil mixture fraction and its RMS variance for varying number of grid cells for finite-rate mixing (C_Φ = 1), (a) radial profiles along XZ-plane at 0.5 m riser height and (b) radially averaged axial profiles (symbols: ◇ - N_p = 10; □ - N_p = 20; △ - N_p = 50; × - N_p = 100), using 965 grid cells and 0.005 s time step (see Eq. 28).

Operating conditions: see Table 1.

The small-scale riser simulation results are summarized as follows, before presenting the full-scale riser simulation results. The presented simulated results for both the grid cells (965 and 1930) and different notional particles in each grid cell (10, 20, 50, and 100) indicate that 965 grid cells suffice to perform the simulations with a lower computational time when compared with the 1930 grid cells. The presented simulation results based on the different notional particles show that 20 notional particles suffice to perform the simulations with a good accuracy and a low computational time. The presented simulated results performed for both the time steps of 0.001 and 0.005 s, using a 965 grid cells and a 20 notional particles finally illustrate that a 0.005-s time step suffices to perform simulations with a good accuracy and a low computational time.

Full-scale riser simulations, using 12,931 grid cells, 20 notional particles, and a time step of 0.005 s are performed. The chosen number of grid cells is based on the scale up of the small-scale riser (with 965 grid cells) to the full-scale riser. A denser grid is implemented at the bottom of the riser where flow density variations are more pronounced due to the high-conversion of the heavy petroleum fractions to lighter products.

Results and Discussion

Hydrodynamics

Figure 10 shows the axial profiles of the solids volume fraction (i) and the solids velocity (ii) in a vertical plane through the middle of the two riser outlets. From Figure 10a, it can be decided that the solids volume fraction rises near the wall and annular flow is observed as in Das et al.[3] As seen in Figure 10b, the solids velocity is found to increase over the riser height. This is a consequence of, (i) the cracking of the heavy gas oil into low molecular weight components such as gasoline, LPG, and dry gas,[29,30,31] (ii) a higher annular region thickness (see Figure 10b) in the top section of the riser decreasing the effective flow area significantly, and (iii) the

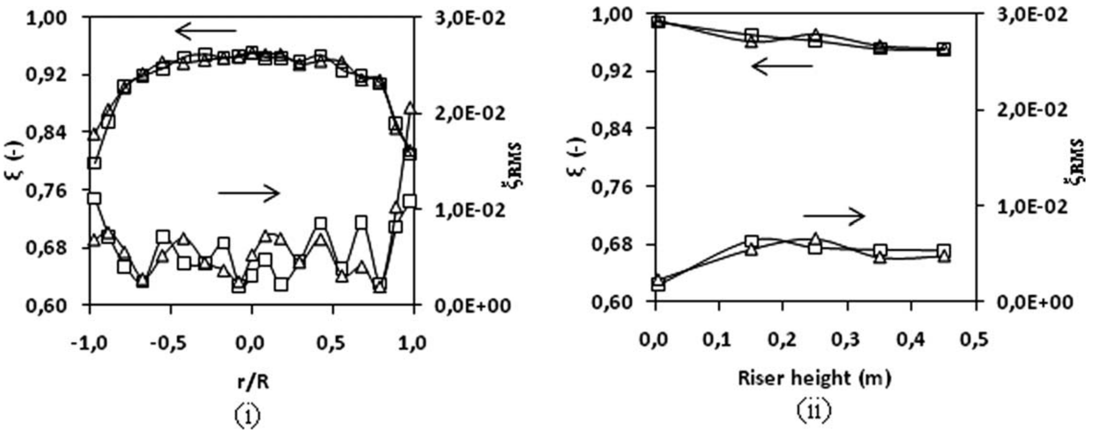

Figure 9. Heavy gas oil mixture fraction and its RMS variance for varying number of grid cells for a finite-rate mixing (C_Φ = 1), (a) radial profiles along *xz*-plane at 0.5 m riser height and (b) radially averaged axial profiles along riser height, (Symbols: □ - dt = 0.005 s; △ - dt = 0.001 s), using 965 grid cells and N_p = 20 (see Eq. 28).

Operating conditions: see Table 1.

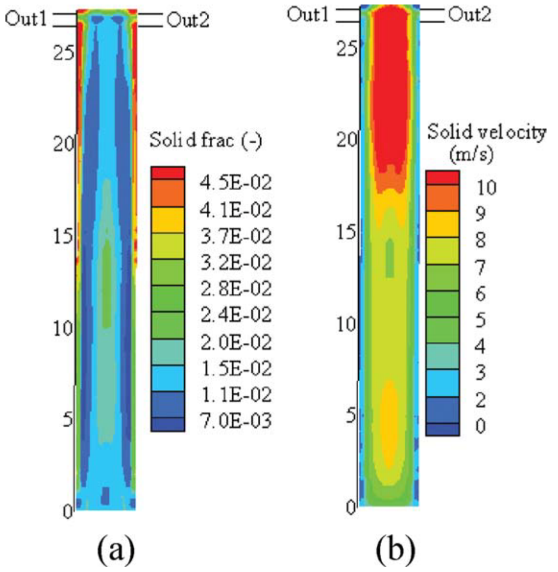

(a) (b)

Figure 10. Fields of (a) solids volume fraction and (b) solids velocity in a cross section through the outlets.

Steady-state simulation (see equations in Tables 1 to 3 in Das et al.[10]). (G_s = 79.0 kg m^{-2} s^{-1}; u_g = 4.55 m s^{-1}; Θ_{in} = 0.14 m^{-2} s^{-2}). Operating conditions: see Table 1. [Color figure can be viewed in the online issue, which is available at wileyonlinelibrary.com.]

gas-phase pressure in the top section of the riser being lower than the bottom value due to the hydrostatic head of the solid. A low-pressure in the top section of the riser increases the velocity of the gas phase when compared with the velocity of the gas phase in the bottom section of the riser.

The radial profiles of the solids' volume fraction, solids velocity, solids granular temperature, total kinetic energy of the gas, dissipation of this kinetic energy of the gas, and gas phase pressure drop at different heights of the riser are shown in Figure 11. To start with, the profiles at a riser height of 10.5 m are discussed, as the riser flow is fully developed at this riser height. The profiles are not influenced by inlet or outlet effects. The solids volume fraction (see Figure 11a) is found to be very high near the riser wall. Going toward the center of the riser, the solids volume fraction goes through a minimum and then rises to higher values in the centre of the riser. Clearly, there are three zones in the riser,[32] referred to as the near-wall region, the annular region, and the core region.[33] The solids volume fraction profile and the solids velocity profile (see Figure 11b) are as expected: a higher solids velocity is calculated in the core region when compared with the annular region. The presence of three regions is mainly attributed to the relatively low granular temperature in the core region of the riser at this riser height (see Figure 11c). A low granular temperature implies a low fluctuating velocity of the solid phase which, in turn, results in an increase of the solids volume fraction and a corresponding decrease of the solids velocity (see Figures 10b and 11b). One must further note the similarity of the off-center peaks of the granular temperature θ (see Figure 11c) and the gas phase turbulent energy k (see Figure 11d) at $r/R = 0.7$ (annular region) resulting in a shift of the solids from the annular region toward the core region and the wall region. This shift is (partially) responsible for the increased solids volume fraction in the core region.

In the riser outlet section, the solids volume fraction profile (see Figure 11a) with three regions is no longer observed. Near the riser outlet, the solids volume fraction in the wall region is low due to the riser outlet effects. The highest value of the solids volume fraction is now calculated in the annular region, and the thickness of this region is significant when compared with the other regions. The latter is a direct consequence of using a "*T*" outlet, resulting in a considerable increase of the solids volume fraction in the top of the riser, as also reported by Das et al.[3]

Finally, in the inlet zone, the solids volume fraction profile (see Figure 11a) is found to be radially more uniform. This corresponds with the radially more uniform profile of the solids velocity (see Figure 11b) near the riser inlet.

As seen in Figures 11d, e, the total kinetic energy of the gas and the dissipation of this kinetic energy increases with the height of the riser due to the rise of velocities and outlet effects. As seen in Figure 11f, the predicted radial gas-phase pressure drop at different heights is uniform.

As seen in Figure 12, the temperature difference between the gas and solid phase temperature is negligible from 1-m riser height on because of the high-rate of heat transfer between both phases.

Species concentrations using the IEM model

The IEM model parameter, that is, mechanical-to-scalar time-scale ratio, (C_Φ) value is taken equal to 2, based on local equilibrium between production and dissipation of the scalar variances.[19] Explicitly, the values for the production and the dissipation of the scalar variances are not known. In this article, the IEM model parameter is chosen to be one. This value is justified based on the high molecular weights of the gases in FCC, which indeed restricts the mixing performance compared to lighter molecular gases as in Vegendla et al.[6] Moreover, this is a tuning parameter, which varies from process to process.

In Table 3, the outlet yields calculated using the new hybrid solution algorithm is compared with the available plant data,[2] and the simulation results when using a RANS approach.[3]

These yields are obtained from

$$Z_j = \frac{X_j \varepsilon_g \rho_g |\boldsymbol{u}|}{C_C \varepsilon_s \rho_s |\boldsymbol{v}| + \sum_j^{m-1} \left(X_j \varepsilon_g \rho_g |\boldsymbol{u}| \right)} \tag{29}$$

The cup-mixing averaged outlet yields are obtained from

$$Z_{j,avg} = \frac{\int Z_j u_z dS}{\int u_z dS} \tag{30}$$

The heavy gas oil is composed of four gaseous lumps representing the paraffinic, naphthenic, aromatic substituent ring, and aromatic ring carbon components. The riser feed is described in terms of these four lumps. The predicted yield of the heavy gas oil over the riser height is shown in Figure 13a. From the analysis of this field, it can be decided that the maximum cracking rate of the heavy gas oil feed to the middle and light gaseous lumps is calculated from the inlet to the middle section of the riser. As seen in Table 3, the

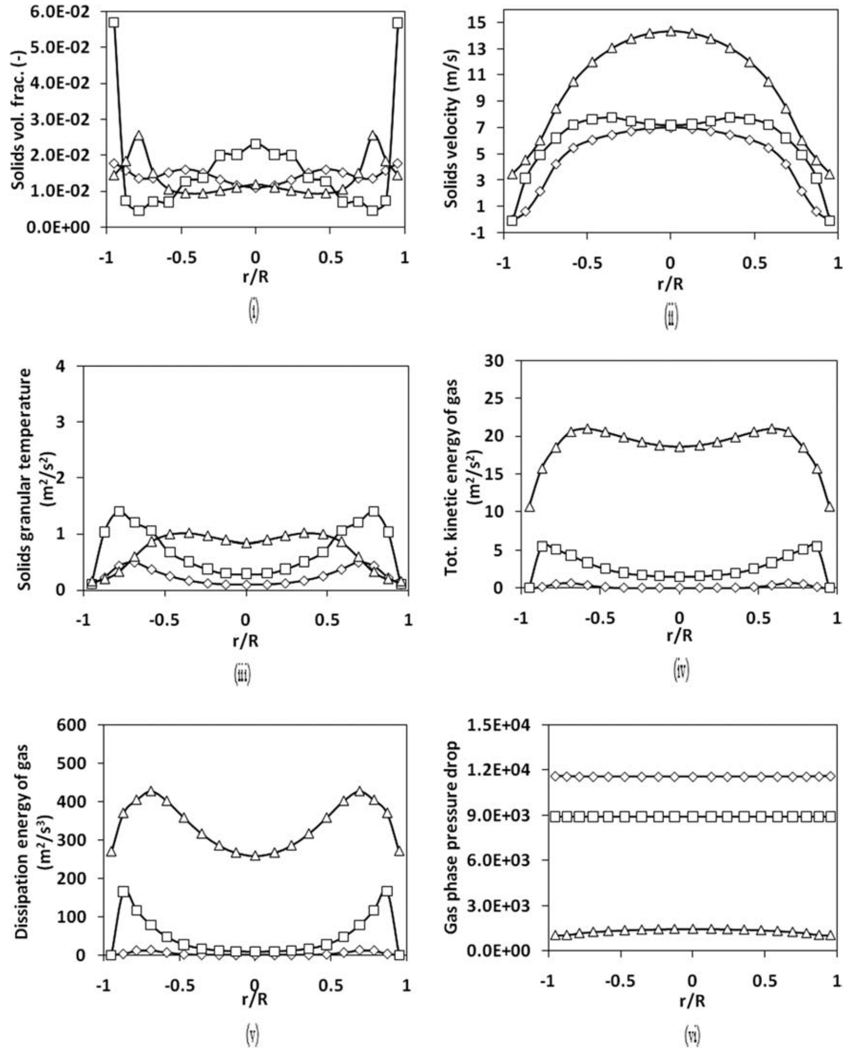

Figure 11. Radial profiles at different heights of the riser, (symbols: ◇ - 1.17 m; □ - 10.5 m; △ - 26.8 m) (a) solids volume fraction, (b) solids velocity, (c) solids granular temperature, (d) total kinetic energy of gas, (e) dissipation energy of gas, and (f) gas phase pressure drop, in a cross-section through the riser outlets (see equations in Tables 1 to 3 in Das et al.[10]).

Operating conditions: see Table 1.

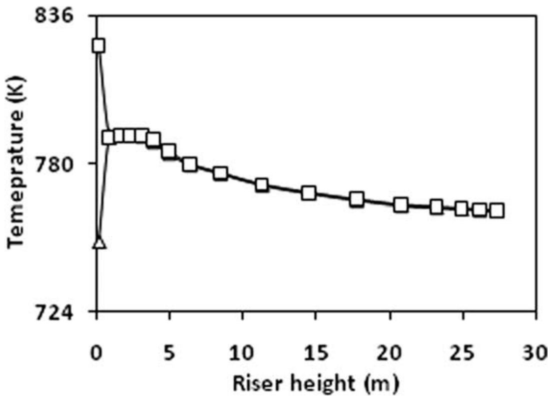

Figure 12. Axial temperature profiles along the riser for gas phase (△) and solids phase (□) for finite-rate mixing ($C_\Phi = 1$) (see Eqs. 18 and 19).

Operating conditions: see Table 1.

predicted outlet yield for the heavy gas oil compares very well with the experimental observation, that is, the conversion of the feed is well predicted.

The medium gas oil is composed of four lumps: medium paraffinic, medium naphthenic, medium aromatic substituent ring, and medium aromatic ring carbon components. The formation of these lumps in a riser reactor is purely due to the cracking of heavy gas oil as can be concluded from the 12-lump kinetic model (see Figure 6). As seen in Figure 13b, the medium gas oil yield rises along the entire height of the riser reactor. As seen in Table 3, the outlet yield is underpredicted. The latter can be due to a slight undercracking of the heavy gas oil to the medium gas oil in the present simulation or a slight overcracking of the medium gas oil itself. A rise of the medium gas oil yield can possibly be obtained by adjusting the mechanical-to-scalar time-scale ratio C_Φ, the IEM model parameter.

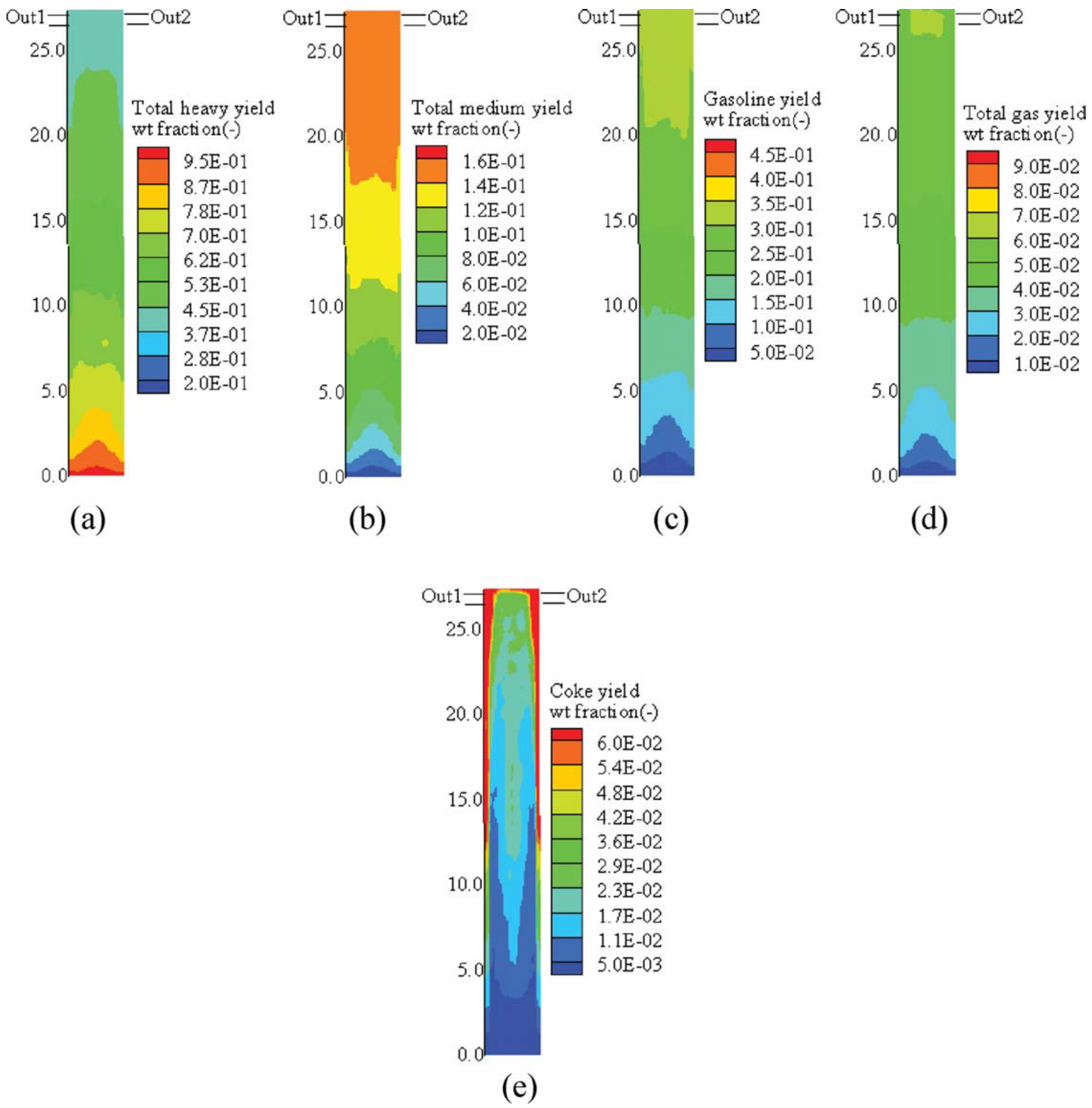

Figure 13. Fields of (a) heavy gas oil, (b) medium gas oil, (c) gasoline, (d) total gas, and (e) coke yield in a cross section through the riser outlets (C_φ = 1) (see Eqs. 16 and 17).

Operating conditions: see Table 1. [Color figure can be viewed in the online issue, which is available at wileyonlinelibrary.com.]

Gasoline is the preferred gaseous product in the FCC riser operation. The gasoline is obtained through the cracking of the heavy and medium gas oil as seen in the 12-lump kinetic scheme (see Figure 6). From the analysis (Figure 13c), it is found that the maximum rise of the gasoline is calculated near the riser inlet section. The formation of the gasoline is overpredicted as seen in Table 3. This can be due to the overcracking of the medium gas oil.

Table 3. Predicted (Eq. 30) vs. Actual Yields at the Riser Exit

Outlet Values	This Work ($C_\Phi = 1.0$)	This Work ($C_\Phi = \infty$)	Plant[2]	RANS[3]
Heavy gas oil yield (wt %)	40.7	38.7	40.4	39.8
Medium gas oil yield (wt %)	15.79	16.0	18.8	16.2
Gasoline yield (wt %)	33.78	35.1	29.7	35
Total gas yield (wt %)	6.25	6.3	7.8	7.0
Coke yield (wt %)	3.45	3.9	3.3	2.0
Temperature (K)	763	758	769	–

The light gaseous (total gas) products in the FCC riser operation are composed of two lumps (LPG and light gas). As seen in Table 3, the outlet yield of the "total gas" is underpredicted. The latter is mainly due to outlet effects as described above. An increase of the coke deposition on the catalyst is a consequence of this underpredicted outlet value. The yield of the "total gas" along the length of the riser is shown in Figure 13d.

The coke formation is mainly due to the cracking of three lumps, namely the heavy aromatic carbon rings, the medium aromatic carbon rings, and the light gases. The formation of the coke on the catalyst along the riser height is shown in Figure 13e. The outlet yield is overpredicted when compared with the experimental observation found in Table 3. The coke formation decreases the catalyst activity. As a consequence, the cracking rate is reduced with riser height.

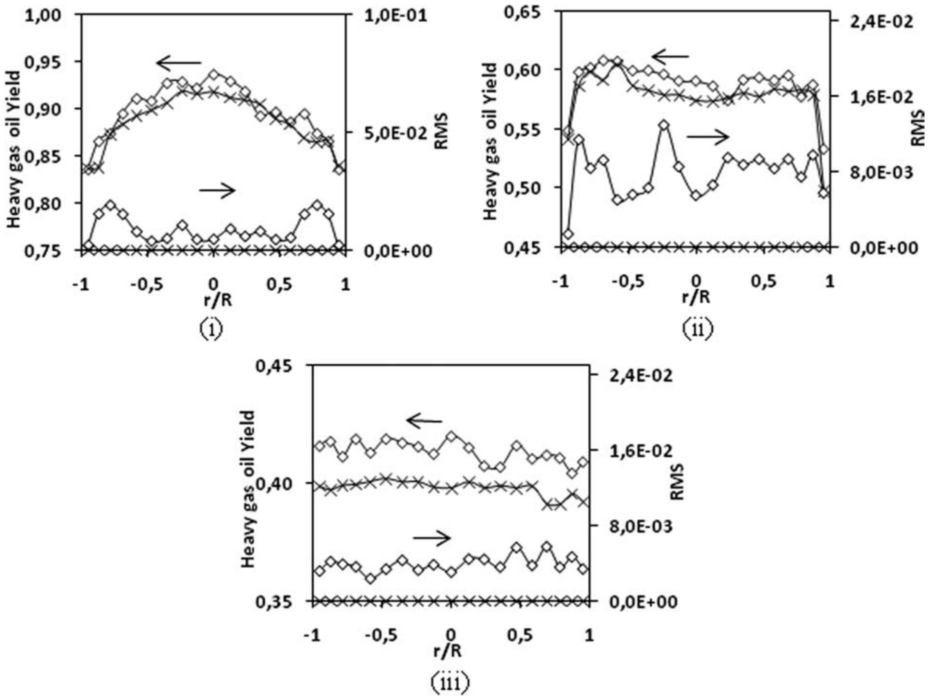

Figure 14. Radial profiles of heavy gas oil (Eq. 29) at different heights of the riser (a) 1.17 m, (b) 10.5 m, and (c) 26.8 in a cross section through the riser outlets (see Eq. 16).

Finite-rate mixing (◇) and infinite-rate mixing (×). Calculated root mean square (RMS) or variance profiles (Eq. 12). Operating conditions: see Table 1.

Effect of mixing model parameter C_Φ

The effect of the IEM mixing model and its parameter dependency, C_Φ, that is, mechanical-to-scalar time-scale ratio, on the predicted yields are studied using a finite and an infinite-rate mixing model. Two reactor simulations are performed using the finite-rate and the infinite-rate mixing model, respectively. For the finite-rate mixing model, the model parameter (C_Φ) is taken as 1. For the infinite-rate mixing model, the model parameter is chosen such that the mixing term in the equations becomes infinitely high ($C_\Phi = \infty$). Applying the infinite-rate mixing model in the PDF method replicates the FV reactor model, that is, average species concentration fluctuations are set equal to zero. From the calculation results presented in the Figures 14–16, it is clear that the use of the finite or the infinite-rate mixing model strongly influences the calculated heavy gas oil, gasoline, and coke yield profiles over the riser height. This is also true for the medium gas oil and the total amount of gases (not shown). When using an infinite-rate mixing model, the calculated yields of heavy gas oil (see Figure 14 and Table 3) are considerably underpredicted, or the conversion is seriously overpredicted, when compared with the yields when using a finite-rate mixing model. Hence, gasoline and coke will be over predicted (Figures 15 and 16). The use of a completely mixed model, that is, infinite-rate mixing model, for the subgrid scalar field, thus, results in high-rates for the feed lumps.

The radial variance profiles (see Eq. 12) for the heavy gas oil, gasoline, and coke are also presented in Figures 14–16. As seen in Figure 14a–c, considerable values are calculated when applying finite-rate mixing. On the other hand, the variance values are zero for infinite-rate mixing confirming the accuracy of the calculations. The variance values for the finite-rate mixing model drop along the riser height (see Figure 14a–c). This reduction is due to the rising conversion of the heavy gas oil along the riser. For medium gas oil (not shown), gasoline, total gas (not shown), and coke, the inverse situation is observed. Variance values for medium gas oil (not shown), gasoline, total gas (not shown), and coke rise toward the top of the riser (see Figures 15 and 16). This is mainly due to their formation along the riser height.

As seen in Figure 17, a lower gas temperature is predicted when using infinite-rate mixing as compared to finite-rate mixing. The variance profiles for finite and infinite-rate mixing are almost zero except near the inlet for the finite-rate mixing model. At the inlet, the variance value seen ~10 K is calculated for finite-rate mixing. The non-zero inlet value is due to the heat transfer from solids to gas, which is limiting (Eq. 18) at the inlet as shown in Figure 12.

In Table 3, the calculated results using the finite and the infinite-rate mixing model are compared with the plant data. When using an infinite-rate mixing model, the outlet yield of heavy gas oil is underpredicted when compared with the finite-rate mixing model results and the plant data. The simulation results for medium gas oil compare very well for both models but are underpredicted when compared with the plant data. Hence, the gasoline, the total amount of gases, and the coke yields are over predicted. Based on the lower feed conversion, the use of the finite-rate mixing model will result in a higher calculated temperature when compared with the infinite-rate mixing model. A difference of 5 K is calculated as seen in Table 3. When compared with experimental

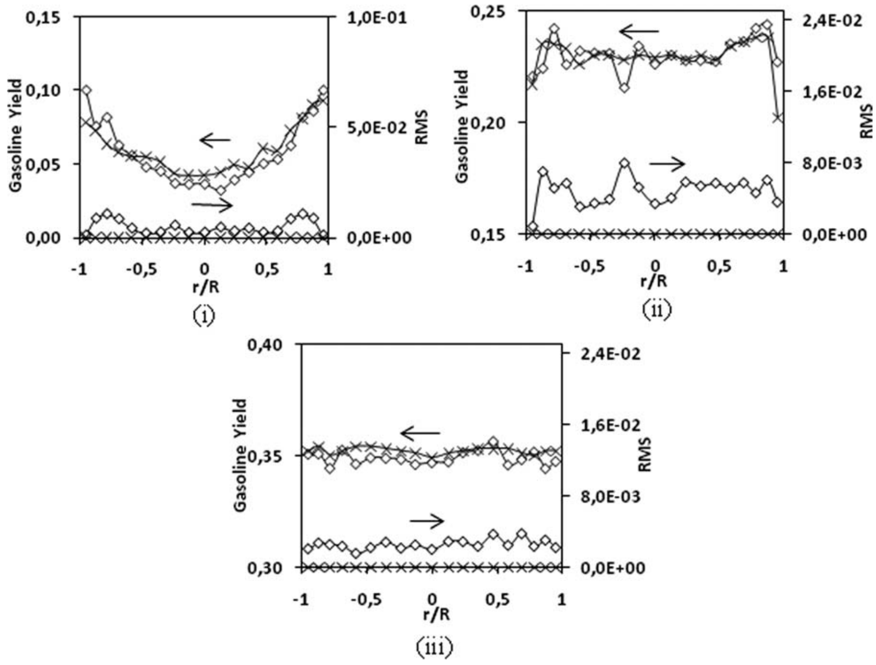

Figure 15. Radial profiles of gasoline (Eq. 29) at different heights of the riser (a) 1.17 m, (b) 10.5 m, and (c) 26.8 in a cross section through the riser outlets (see Eq. 16).

Finite-rate mixing (◇) and infinite-rate mixing (×). Calculated root mean square (RMS) or variance profiles (Eq. 12). Operating conditions: see Table 1.

values, the underpredicted temperature of the gas phase and the solid phase is due to the neglecting the catalyst particle–particle and particle-wall collisions in the modeled equations as mentioned above.

As seen in Table 3, the overall performance of the presented hybrid algorithm is high. Results calculated, when considering finite-rate mixing in the simulation model, are quantitatively comparable with the pilot plant yields. The

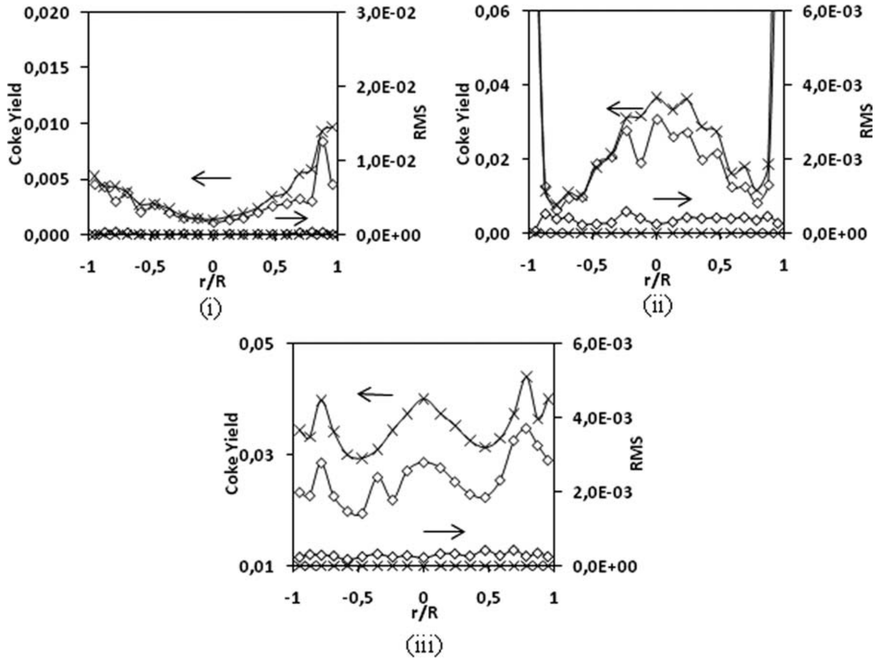

Figure 16. Radial profiles of coke (Eq. 29) at different heights of the riser (a) 1.17 m, (b) 10.5 m, and (c) 26.8 in a cross section through the riser outlets (see Eq. 17).

No mixing (◇) and infinite-rate mixing (×). Calculated root mean square (RMS) or variance profiles (Eq. 12). Operating conditions: see Table 1.

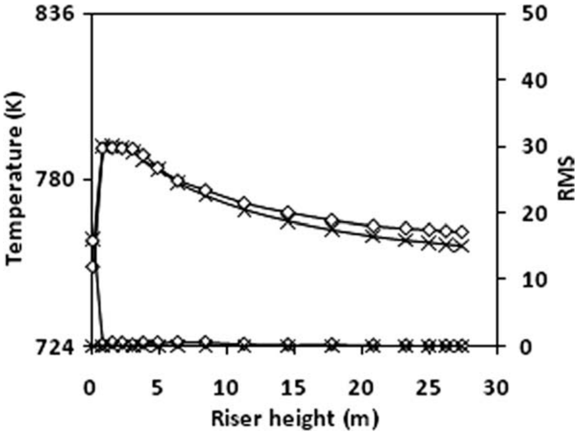

Figure 17. Axial riser gas temperature profiles for finite and infinite-rate mixing (see Eqs. 18 and 19).

Finite-rate mixing (◇) and infinite-rate mixing (×). Calculated root mean square (RMS) or variance profiles (Eq. 12). Operating conditions: see Table 1.

results calculated, when considering an infinite-rate mixing in the simulation model, are found to deviate more from the pilot plant yields. This is due to a high-conversion of the feed, due to high reaction rates.

In Table 3, the calculated gasoline yield obtained when considering infinite rate mixing and when using the conventional methods (RANS) are comparable. On the other hand, the heavy gas oil yield, the medium gas yield and the total gas yield are slightly underpredicted when compared with the RANS approach. The cokes yield is exceptionally well predicted using the finite rate mixing method. The above deviations between the RANS approach and the plant data could be due to the numerical solution technique and to the fact that the temperature profiles obtained from 1D simulation results as discussed in Das et al.,[3] are imposed. The RANS equations are solved using the Eulerian method, which is numerically more diffusive than the Lagrangian method.

As discussed in the Introduction section, the novelty of this work is the application of the transported scalar PDF method, which allows treating the highly nonlinear chemical source terms in the species continuity equations without the need for closure. On the contrary, the RANS and LES methods require closures for these chemical source terms or infinite rate mixing conditions need to be assumed to neglect the turbulent fluctuations of these chemical source terms.

Conclusions

With the in-house developed CFD code FLOWMER-PDF, a new hybrid solution algorithm to solve the set of conservation equations in an FCC riser is developed. The conservation equations for total mass and momentum for both phases are solved using a FV technique. The species continuity equations are formulated using a PDF method. The use of the PDF method avoids the need to model the reaction source term in the species continuity equations. Instead, the modeling effort shifts to the mesomixing and micromixing contributions in the PDF equations. The former is closed by using the gradient-diffusion model, whereas the latter is accounted by using the IEM model. SDEs are introduced as replicas of the transported composition PDF equations. A notional-particle-based MC technique is used to solve these SDEs, thus, determining the position and the composition of the computational particles. The simulations are performed using a 12-lump FCC kinetic model. The calculated product yields are in good agreement with the experimentally observed product outlet yields. An IEM mixing model parameter C_Φ value of 1 is found to be adequate to describe the FCC riser reactive flow. A strong effect of using a finite-rate mixing model as compared to an infinite-rate mixing model is observed, especially for the calculated conversion of the FCC feed. Using the finite-rate mixing model gives a good agreement between the calculated yields and reported pilot plant data.

Notation

a_m = external solid surface area, ($\mathrm{m^2\ kg^{-1}_{catalyst}}$)
C = specific heat, ($\mathrm{J\ kg^{-1}\ K^{-1}}$)
C_c = mass fraction of coke, ($\mathrm{kg_{coke}\ kg^{-1}_{catalyst}}$)
C_Φ = mechanical-to-scalar time-scale ratio, (-)
D = molecular diffusivity, ($\mathrm{m^2\ s^{-1}}$)
d = distance, (m)
f_φ = scalar probability density function, (-)
G = mass flux, ($\mathrm{kg\ m^{-2}\ s^{-1}}$)
h_gs = heat-transfer coefficient in gas-solid interface, ($\mathrm{J\ m^{-2}\ s^{-1}}$)
ΔH_rxn = heat of reaction, ($\mathrm{J\ kg^{-1}}$)
k = turbulent kinetic energy for gas phase, ($\mathrm{m^2\ s^{-2}}$) (or) reaction rate coefficient, ($\mathrm{m^3\ kg^{-1}_{catalyst}\ kg^{-1}_{catalyst}\ s^{-1}}$)
K = equilibrium adsorption coefficient, (-)
k_gs = mass transfer coefficient in gas-solid interface, ($\mathrm{mol\ m^{-2}\ s^{-1}}$)
M = molecular mass, ($\mathrm{kg\ mol^{-1}}$)
m = number of paths, (-) (or) mass of notional-particle, (kg)
N = number of notional particles, (-)
N_TA = number of time-averaged iterations, (-)
P = total pressure, ($\mathrm{kg\ m^{-1}\ s^{-2}}$)
R = universal gas constant, ($\mathrm{m^3\ Pa\ K^{-1}\ mol^{-1}}$)
R_j = reaction source term for component j, ($\mathrm{mol\ m^{-3}\ s^{-1}}$)
r = net production rate, ($\mathrm{mol\ kg^{-1}_{catalyst}\ s^{-1}}$)
S_gs = mass transfer term, ($\mathrm{mol\ m^{-3}\ s^{-1}}$) (or) heat-transfer term, ($\mathrm{K\ s^{-1}}$)
Sc = Schmidt number, [$\mu/((D)$], (-)
t = time, (s)
T = temperature, (K)
$\mathbf{u}$ = interstitial gas velocity vector, ($\mathrm{m^3_{gas}\ m^{-2}_{reactor}\ s^{-1}}$)
$\mathbf{v}$ = interstitial solid velocity vector, ($\mathrm{m^3_{solid}\ m^{-2}_{reactor}\ s^{-1}}$)
$\mathbf{y},\mathbf{Y}$ = position vector, (m)
$\mathrm{d}\mathbf{W}$ = Wiener diffusion, ($\mathrm{s^{-1/2}}$)
$\mathbf{w}$ = weighing factor, (-)
X = mass fraction, (-)
$\mathbf{Z}$ = state vector consists of composition and space variables
Z = yield, (-)

Greek letters

φ = vector of scalars, that is, composition or temperature, ($\mathrm{mol\ m^{-3}}$ or K)
φ_α = scalar variable, that is, composition or temperature, ($\mathrm{mol\ m^{-3}}$ or K)
φ_c = activity of catalyst, (-)
θ = granular kinetic energy, ($\mathrm{m^2\ s^{-2}}$)
ρ = density, ($\mathrm{kg\ m^{-3}}$)
μ = viscosity of the gas or solid, ($\mathrm{kg\ m^{-1}\ s^{-1}}$)
υ = carbon number of heavy gas oil, (-)
$\varepsilon_\mathrm{g/s}$ = gas (or) solid volume fraction of the riser, ($\mathrm{m^3_{gas/solid}\ m^{-3}_{reactor}}$)
ε = turbulent dissipation energy for gas phase, ($\mathrm{m^2\ s^{-3}}$)
τ_Φ, τ_u = micromixing and integral time scale, (s)
ψ

= vector of scalars, that is, composition or temperature, (mol m^{-3} or K)

ψ_α = scalar variable, that is, composition or temperature, (mol m^{-3} or K)

ξ = standardized joint normal random vector, (-)

ξ = mean mixture fraction, (-)

γ = stoichiometric coefficient, (-)

δ_{ij} = indicator function, (-)

Subscripts

avg = average
b = basis
g = gas
G = gasoline
h = heavy
in = inlet
j = indices
l = grid cell number
L = light gases
m = medium
o = initial
RMS = Root mean square
s,p = solid phase (or) path indices
sim = simulation
TA = time average
α = scalar component
var = variance
z = axial direction

Superscripts

i = iteration number
n = indices
ng = *n*th notional particle for gas
ns = *n*th notional particle for solid
t = turbulent
$\sim$ = density-weighted mean
$''$ = fluctuation about density-weighted mean

Literature Cited

1. Jenny P, Pope SB, Muradoglu M, Caughey DA. A hybrid algorithm for the joint PDF equation of turbulent reactive flows. *J Comput Phys*. 2001;166:218–252.
2. Gao J, Xu C, Lin S, Yang G, Guo Y. Advanced model for turbulent gas-solid flow and reaction in FCC riser reactors. *AIChE J*. 1999;45:1095–1113.
3. Das AK, Baudrez E, Marin GB, Heynderickx GJ. Three-dimensional simulation of a fluid catalytic cracking riser reactor. *Ind Eng Chem Res*. 2003;42:2602–2617.
4. Agrawal K, Loezos PN, Syamlal M, Sundaresan S. The role of meso-scale structures in rapid gas-solid flows. *J Fluid Mech*. 2001;445:151–185.
5. Fox RO. *Computational Models for Turbulent Reacting Flows*. Cambridge, UK: Cambridge University Press, 2003:1–419.
6. Vegendla SNP, Heynderickx GJ, Marin GB. Probability density function simulation of turbulent reactive gas-solid flow in a riser. *Chem Eng Technol*. 2009;32:492–500.
7. Kolhapure NH, Fox RO, Daiss A, Maehling FO. PDF simulation of ethylene decomposition in tubular LDPE reactors. *AIChE J*. 2005;51:585–606.
8. De Wilde J, Marin GB, Heynderickx GJ. The effects of abrupt T-outlets in a riser: 3D simulation using the kinetic theory of granular flow. *Chem Eng Sci*. 2003;58:877–885.
9. De Wilde J, Vierendeels J, Heynderickx GJ, Marin GB. Simultaneous solution algorithms for Eulerian-Eulerian gas-solid flow models: stability analysis and convergence behavior of a point and a plane solver. *J Comput Phys*. 2005;207:309–353.
10. Das AK, De Wilde J, Heynderickx GJ, Marin GB, Vierendeels J, Dick E. CFD simulation of dilute phase gas-solid riser reactors: part I—a new solution method and flow model validation. *Chem Eng Sci*. 2004;59:167–186.
11. De Wilde J, Marin GB. Investigation of simultaneous adsorption of SO_2 and NO_x on Na-γ-Al_2O_3 with transient techniques. *Catal Today*. 2000;62:319–328.
12. De Wilde J, Das AK, Heynderickx GJ, Marin GB. Development of a transient kinetic model for the simultaneous adsorption of SO_2–NO_x over Na-γ-Al2O3 sorbent. *Ind Eng Chem Res*. 2001;40:119–130.
13. Launder BE, Spalding DB. The numerical computation of turbulent flow. *Comp Methods Appl Mech Eng*. 1974;3:269.
14. Gidaspow D. *Multiphase Flow and Fluidization: Continuum and Kinetic Theory Descriptions*. New York: Academic Press, 1994.
15. Minier JP, Peirano E. The PDF approach to turbulent polydispersed two-phase flows. *Phys Rep*. 2001;352:1–214.
16. Martignoni W, de Lasa HI. Heterogeneous reaction model for FCC riser units. *Chem Eng Sci*. 2001;56:605–612.
17. Carrara MD, DesJardin PE. A filtered mass density function approach for modeling separated two-phase flows for LES I: mathematical formulation. *Int J Multiphase Flow*. 2006;32: 365–384.
18. Carrara MD, DesJardin PE. A filtered mass density function approach for modeling separated two-phase flows for LES II: simulation of a droplet laden temporally developing mixing layer. *Int J Multiphase Flow*. 2007;34:748–766.
19. Raman V, Fox RO, Harvey AD. Hybrid finite-volume/transport PDF simulations of a partially premixed methane-air flame. *Combust Flame*. 2004;136:327–350.
20. Cassiani M, Franzese P, Giostra U. A PDF micromixing model of dispersion for atmospheric flow. Part I: development of the model, application to homogeneous turbulence and to neutral boundary layer. *Atmos Environ*. 2005;39:1457–1469.
21. Fox RO. On the relationship between Lagrangian micromixing models and computational fluid dynamics. *Chem Eng Process*. 1998;37:521–535.
22. Apte SV, Mahesh K, Moin P, Oefelein JC. Large-eddy simulation of swirling particle-laden flows in a coaxial-jet combustor. *Int J Multiphase Flow*. 2003;29:1311–1331.
23. Subramaniam S, Haworth DC. A probability density function method for turbulent mixing and combustion on three-dimensional unstructured deforming meshes. *J Engine Res*. 2000;1:171–190.
24. Sadarjoen A, Walsum TV, Hin AJS, Post FH. *Particle tracing algorithms for 3D curvilinear grids*. In: Nielson G,Hagen H, Müller H, editor. *Scientific Visualization: Overviews, Methodologies, and Techniques*. IEEE CS Press. 1997;311–335.
25. Peixoto FC, de Medeiros JL. Reactions in multi-indexed continuous mixtures: catalytic cracking of petroleum fractions. *AIChE J*. 2001;47:935–947.
26. Gao J, Lan X, Fan Y, Chang J, Wang G, Lu C, Xu C. CFD modeling and validation of the turbulent fluidized bed of FCC particles. *AIChE J*. 2009;55:1680–1694.
27. Xu J, Pope SB. Assessment of numerical accuracy of PDF/Monte Carlo methods for turbulent reacting flows. *J Comput Phys*. 1999;152:192–230.
28. Ko GH, Hamins A, Bundy M, Johnsson EL, Kimb SC, Lenhert DB. Mixture fraction analysis of combustion products in the upper layer of reduced-scale compartment fires. *Combust Flame*. 2009;156: 467–476.
29. Benyahia S, Ortiz AG, Paredes JIP. Numerical analysis of a reacting gas/solid flow in the riser section of an industrial fluid catalytic cracking unit. *Int J Chem React Eng*. 2003;1:Article A41.
30. Pareek VK, Adesina AA, Srivastava A, Sharma R. Modeling of a non-isothermal FCC riser. *Chem Eng J*. 2003;92:101–109.
31. Novia N, Ray M, Pareek V. Three-dimensional hydrodynamics and reaction kinetics analysis in FCC riser reactors. *Chem Prod Process Model 2*. 2007;2:Article 4.
32. Chalermsinsuwan B, Piumsomboon P, Gidaspow D. Kinetic theory based computation of PSRI riser: part I—estimate of mass transfer coefficient. *Chem Eng Sci*. 2009;64:1195–1211.
33. Van de Velden M, Baeyens J, Seville JPK, Fan X. The solids flow in the riser of a circulating fluidised bed (CFB) viewed by positron emission particle tracking (PEPT). *Powder Technol*. 2008;183:290–296.

Manuscript received Dec. 24, 2009, revision received Oct. 8, 2010, and final revision received Jan. 13, 2011.